Sustainable Energy & Fuels

ROYAL SOCIETY OF CHEMISTRY

PAPER

View Article Online
View Journal

Cite this: DOI: 10.1039/d1se00444a

ZnO nanoparticle confined stress amplified all-fiber piezoelectric nanogenerator for self-powered healthcare monitoring†

Biswajit Mahanty, ‡[ab] Sujoy Kumar Ghosh, ‡§[a] Santanu Jana,‡[c] Zinnia Mallick,[d] Subrata Sarkar[a] and Dipankar Mandal *[d]

In this work, an all-fiber piezoelectric nanogenerator (A-PNG) is designed by using ZnO nanoparticles (NPs) reinforced poly(vinylidene fluoride) (PVDF) electrospun nanofibers as the active layer and interlocked conducting microfiber composite mats as electrodes to convert the mechanical energy into electrical power. Theoretical simulation using finite element analysis on stress distribution shows that the external stress can be concentrated to deform ZnO nanoparticles by 7.2 fold of magnitude compared to the surrounding neat PVDF, improving the stress-induced large polarization in the resulting PVDF–ZnO composite nanofibers, thus enabling improved generation of electricity. Nano-scale investigation revealed superior generation of ferro- and piezo-electricity using the PVDF–ZnO composite nanofibers, showing an excellent piezoelectric charge coefficient of $d_{33} = -32$ pC N^{-1}. As a result, the A-PNG shows a high electrical throughput, with 18 V of open-circuit output voltage, 26.7 μW cm^{-2} of output power density, and 11.52 × 10^{-12} Pa^{-1} for the piezoelectric figure of merit (FoM). In addition, the excellent mechanical to the electrical energy conversion efficiency of 91%, means that the system is suitable for driving a range of consumer electronics components, such as capacitors and light-emitting diodes (LEDs). The quick response time of 10 ms means it is feasible for ultra-fast signal detection in a healthcare monitoring system. Owing to the skin conformable functionality on different body parts, such as wrists, fingers, throat, and knees, the A-PNG was found to be attractive for application in detecting the pulse rate, muscle behavior, and coughing signal characteristics in order to monitor health conditions. The robust device structure means the A-PNG can be used as a weight monitoring sensor as it is able to predict the weight of a person in a weight range between 45 and 80 kg.

Received 24th March 2021
Accepted 19th July 2021

DOI: 10.1039/d1se00444a

rsc.li/sustainable-energy

1. Introduction

In modern lifestyles, monitoring biomedical systems in real-time has provided significant medical breakthroughs in which standard essential evidence, including vital signs, the respiratory rate, body temperature, muscle behavior, coughing signals, blood pressure measurements, and the main physiological measurements, can be easily collected by health professionals to provide basic knowledge about the human body.[1,2] However, existing medical equipment for the continuous monitoring of human health has serious disadvantages, including inflexible structures,[3] a high power consumption,[4] and limited functionality,[5] causing problems in everyday life, and these issues have prevented medical applications. To solve this challenge, a tremendous amount of on-going research is being performed on the development of ductile medical sensors that present conformal and ultrasensitive functionality with wireless human–machine interactions.[6,7] In this context, researchers have developed flexible pressure sensors that are dependent on different transduction methods such as piezoresistive,[8,9] capacitive,[10,11] electromagnetic,[12] and optical types.[13] These sensors are operated using a constant power supply,[14] which is one of the main barriers to the use of wearable/internet of things (IoT) based sensors.[15,16] The regular replacement of batteries is tedious and they contain chemicals and metals that are toxic, as well as a threat to the environment and to human health, therefore the removal of batteries is tightly regulated. In this scenario, the self-powered pressure sensor is a suitable remedy to solve the power consumption related issues for wearable/IoT based sensors. To achieve this goal it is proposed

[a]Department of Physics, Jadavpur University, Kolkata 700032, India
[b]Department of Electronics & Communication Engineering, Ramgarh Engineering College, Murbanda, Ramgarh, Jharkhand 825101, India
[c]Department of Electronics, Netaji Nagar Day College, Kolkata 700092, India
[d]Quantum Materials and Devices Unit, Institute of Nano Science and Technology, Knowledge City, Sector 81, Mohali 140306, India. E-mail: dmandal@inst.ac.in; dpkrmandal@gmail.com; Fax: +91-172-2211074; Tel: +91-172-2210075

† Electronic supplementary information (ESI) available. See DOI: 10.1039/d1se00444a

‡ These authors contributed equally to this work.

§ Present address: Laboratorio NEST, Istituto Nanoscienze-CNR and Scuola Normale Superiore, Piazza S. Silvestro 12, I-56127 Pisa, Italy.

that piezoelectric[17,18] and triboelectric[19–21] material-based pressure sensors, which generate electricity from environmental mechanical vibrations, could be suitable and could facilitate the accomplishment of a self-powered sensor system. Thus, the sensor behaves as an energy harvester, and is termed a nanogenerator. However, the triboelectric based pressure sensors have some drawbacks compared to those of the piezoelectric based pressure sensors, such as: (i) susceptibility to humidity; (ii) abrasion resistance; and (iii) limited use in bio-signal detection as two dissimilar materials need to effectively interact with each other.[22] Pressure sensors based on inorganic piezoelectric materials[23] have been developed and those reported to date exhibit promising mechanical pressure sensing performances. However, the brittleness, and the complicated and cost-intensive processability, as well as the use of a toxic lead (Pb) constituent as an initial precursor, limit the fabrication of pressure sensors.[24] Organic piezoelectric materials, particularly poly(vinylidene fluoride) (PVDF) (chemical formula: $-(CH_2-CF_2)_n-$) and its copolymers are some of the best candidates owing to their flexibility, light-weight, film-forming capabilities, and chemically stable polymer materials, as well as their suitability for fabricating large surface area and ductile clothing sensors, actuators, energy scavengers, energy sources, and biomedical equipment.[25–27] In this regard, electrospinning-based PVDF nanofibers are *in situ* poled and spatially confined, which generates a higher piezoelectricity in comparison to electrically poled PVDF films.[28] In addition, the nano-filler reinforced PVDF nanofibers possess the synergistic enhancement of the piezoelectric output.[29] Nevertheless, fabricated nano-filler-induced PVDF nanofibrous devices still have a low piezoelectric coefficient (d_{33}) and output efficiency. To solve this issue, inorganic nano-fillers can be used, in particular, low-cost ZnO, which is a biocompatible, non-toxic, easy to grow compound that is abundant in nature, and the shape of which is easy to tailor in all substrates. ZnO a very interesting material owing to the wide range of outstanding electrical and optical properties.[30,31] To date, there have been several reports on nano-fillers (such as, ZnO and BTO) that have been incorporated into PVDF nanofiber composites to improve the electroactive phase content of PVDF, and these are mainly considered as being responsible for the generation of a higher piezoelectric energy.[18,32–35] Still, the overall output performance (in terms of the output voltage, power, efficiency and sensitivity) of the reported devices has not yet reached the required level. An important feature of the energy harvesting device is the electrode. In most of the studies, electrospun fiber based devices were prepared using metal foil electrodes or metal coated thin film electrodes as charge collectors that limit the lifetime of the device under extended cyclic stress.[18,32–37] In addition, the metal electrodes made the devices bulky which restricts the applications of the device for self-powered wearable physiological signal monitoring uses. There were a few more limitations observed, including the fact that the poor fatigue resistance causes early failure of the metal foils, and the huge mismatch in the Young's modulus and Poisson's ratio of the metal coating electrode and the active thin film. However, owing to the prolonged period of application, a loss of mechanical integrity and electric connectivity occurs. As a result, the stress concentration effect[38] between the high modulus ZnO nanoparticles (102.6 GPa)[39] and the low modulus PVDF nanofibers (9 MPa)[29] is often neglected and has not been explored until now. To date, no reports have been published on the stress concentration effect biased improved piezoelectric performance on the PVDF–ZnO nanocomposite based all-fiber textile sensor.

In this work, the limitations of existing devices are avoided by the fabrication of a durable and efficient all fiber nanogenerator three layered structure, in which the piezoelectric active component and electrodes are both composed of flexible and soft fiber arrays. We have explored the stress concentration effect, which induced a very large piezoelectric coefficient, $d_{33} \sim -32$ pC N^{-1}, in the PVDF–ZnO nanocomposite. As a result, stress-induced large polarization was achieved in the PVDF–ZnO nanocomposite, rendering a high piezoelectric throughput. Along with this, a facile and cost-effective approach is presented to design a highly ductile, subtle, and self-powered wearable pressure sensor. As a proof of concept, the possibility of real-time physiological signal monitoring was demonstrated using our epidermal sensor.

2. Results and discussion

2.1. Theoretical investigation

Fig. 1a exhibits the finite element method (FEM) based theoretical simulation in which a PVDF–ZnO nanoparticles (NPs) based composite nanofiber shows a strong stress concentration effect in comparison to neat PVDF and PVDF–ZnO nanorods based composite fibers. The details of the simulation process are discussed in the ESI, Text S1.† A vertical stress amplitude of 18 kPa was applied to the nanofibers as all the boundary conditions are the same in both nanofibers. As stress is mainly concentrated on the higher modulus ZnO (NPs) and transmitted to the overall nanofiber, thus, the overall stress amplitude is amplified in comparison to the applied stress amplitude. An interesting point is that the ZnO nanoparticles concentrated more stress than the ZnO nanorods at the same Young's modulus. For example, the amplified maximum stress amplitude in the PVDF–ZnO NPs based composite nanofiber was 2 MPa, which is higher than that of the PVDF–ZnO nanorod based composite nanofiber (~0.75 MPa) and the neat PVDF nanofiber (~0.28 MPa). In the case of the neat PVDF nanofiber, the applied stress is quickly attenuated to the lower electrode region, and the maximum stress is amplified to the lower part of the nanofiber, not to the overall nanofiber. To quantify this stress concentration effect, we estimated the stress concentration factor (K_t), which is the ratio of the amplified stress generated (σ_g) to the applied stress (σ_a): $K_t \approx \frac{\sigma_g}{\sigma_a}$. The K_t value of approximately 111 for the PVDF–ZnO nanoparticle composite nanofiber is 2.7 fold higher than that of the PVDF–ZnO nanorod-based composite nanofiber ($K_t \sim 41.7$) and 7.2 fold higher than that of the neat PVDF ($K_t \sim 15.5$) nanofiber. Considering a single interaction point of the ZnO NP and PVDF fiber, it has been observed that this stress amplification phenomenon is linear and much higher in higher stress

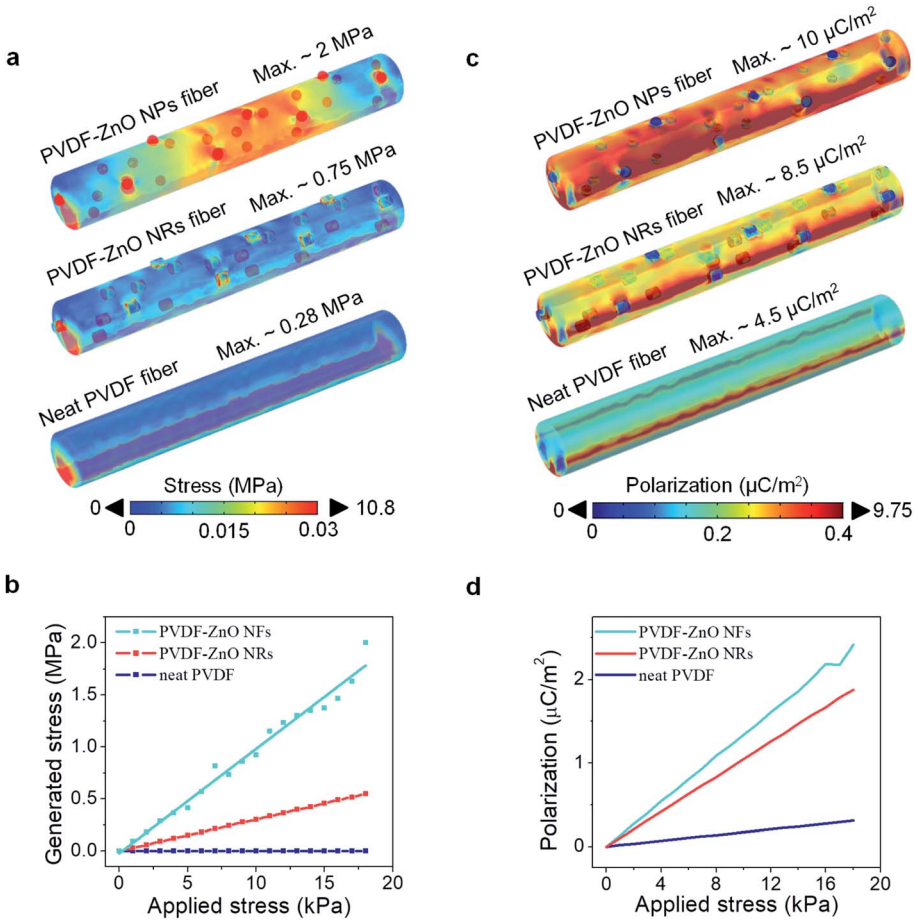

Fig. 1 Theoretical simulation of the stress concentration effect. (a) Internal generated stress in the PVDF–ZnO composite nanofibers, PVDF–ZnO nanorods, and neat PVDF nanofibers. (b) The variation of the applied stress *versus* the generated stress of the PVDF–ZnO composite nanofibers, PVDF–ZnO nanorods, and neat PVDF nanofibers. (c) Internal generated polarization in PVDF–ZnO composite nanofibers, PVDF–ZnO nanorods, and neat PVDF nanofibers with applied stress. (d) The polarization *versus* applied stress for PVDF–ZnO composite nanofibers, PVDF–ZnO nanorods, and neat PVDF nanofibers.

regions, as shown in Fig. 1b. Accordingly, the stress-induced large polarization is achieved in the PVDF–ZnO NPs based composite nanofiber (~9.75 μC m^{-2}), in comparison to the PVDF–ZnO NRs based composite nanofiber (~8.5 μC m^{-2}) and the neat PVDF nanofiber (~4.5 μC m^{-2}) (Fig. 1c). In this case, the polarization was higher in the nanofiber region than that in the ZnO region. In addition, a linear improvement of the polarization was noticed with the increase in pressure, considering one interaction point in the fiber (Fig. 1d). This stress-induced polarization in turn contributes to the overall energy harvesting process. As a result, this theoretical investigation provides evidence of the suitability of the ZnO NPs as effective fillers for improving the energy harvesting process in the PVDF nanofibers based energy harvesters.

2.2. Structural assessment

In order to investigate the suitability of this theoretical prediction, an all-fiber piezoelectric nanogenerator (A-PNG) was prepared (Fig. 2a) using copper (Cu)–nickel (Ni) plated interlocked microfiber based polyester fabric (Fig. 2b) as the top and bottom electrodes for charge collection and PVDF–ZnO NPs based composite nanofibers as an active piezoelectric component (Fig. 2b). The transmission electron microscopy (TEM) image of the PVDF–ZnO composite nanofiber (Fig. 2c) shows that ZnO NPs were nicely accommodated within the PVDF nanofiber. To fabricate the PVDF–ZnO composite nanofiber, the ZnO NPs were first synthesized using a low temperature hydrothermal synthesis route (details and processes are explained in the experimental section). The X-ray diffractometry (XRD) patterns for the ZnO nanoparticle powder (Fig. S1a, ESI†) correspond to the hexagonal wurtzite structure (JCPDS card no. 36-1451).[18] Additionally, the TEM image of a single ZnO nanoparticle shows directly visualized lattice *d*-spacings of 0.26 nm corresponding to the (101) lattice planes. Additionally, from the field emission scanning electron microscopy (FE-SEM) images (Fig. S2, ESI†), it has been observed that the PVDF–ZnO composite nanofibers possess a reduced fiber diameter (~150 nm) compared to that of the neat PVDF nanofibers (~289 nm). This generally occurs as a result of the increase in viscosity and conductivity of the PVDF solution after mixing the nano-fillers.[18] The decrease in the fiber diameter indicates more spatially confined polarization, which is promising for energy harvesting

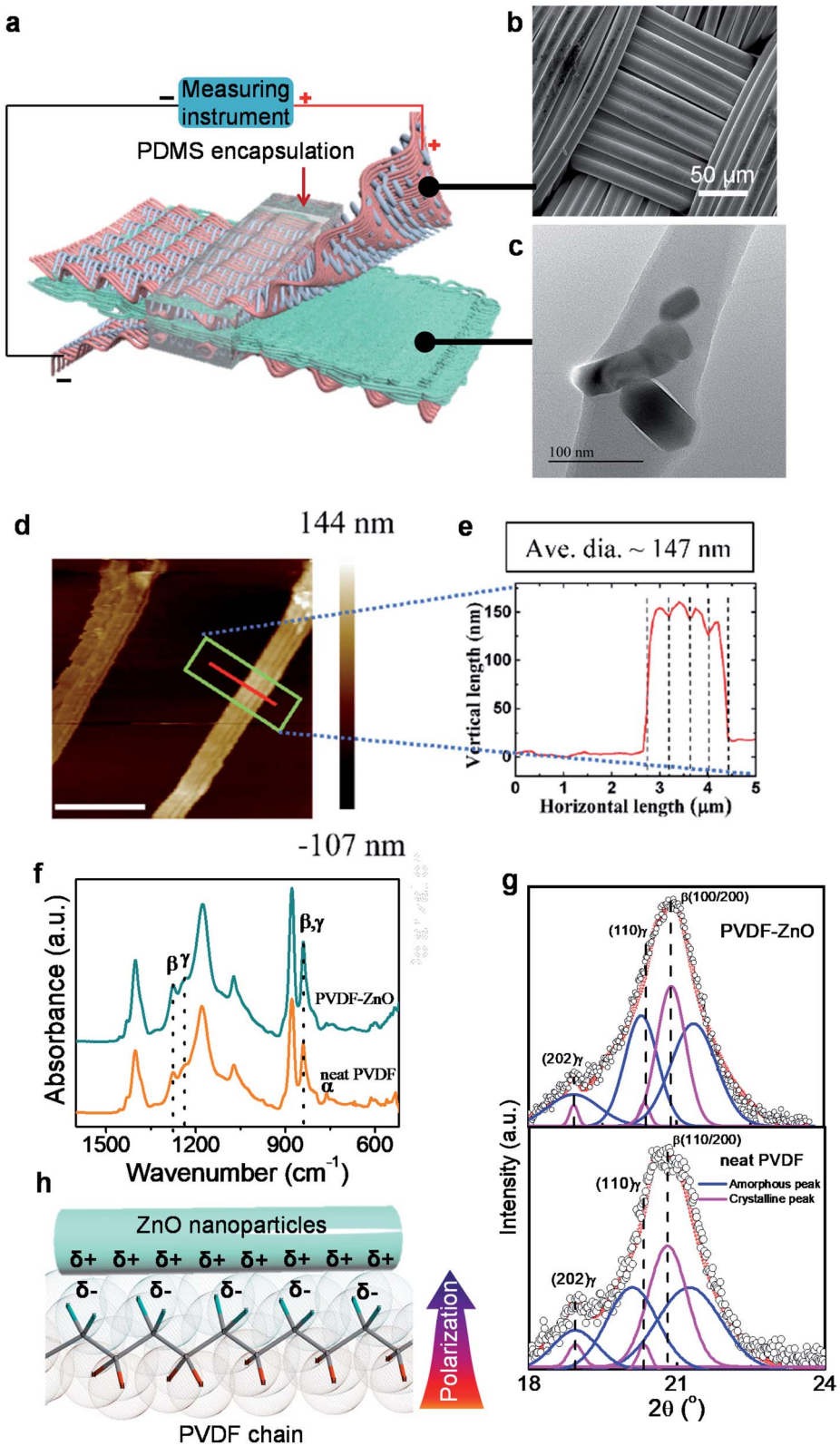

Fig. 2 (a) Schematic diagram of the all-fiber A-PNG. (b) Micro-fiber based conducting fabric electrode. (c) TEM images of the PVDF–ZnO composite nanofiber as an active material. (d) AFM topography image of the overlapping nanofibers (scale bar: 5 μm), and (e) the corresponding line scan showing the diameter of the nanofibers. (f) FT-IR spectra of neat PVDF and the PVDF–ZnO composite nanofibers mat in the wavenumber region from 1600 to 400 cm^{-1}. (g) XRD patterns and their curve deconvolution for neat PVDF and the PVDF–ZnO composite nanofibers mat. The dotted points show the experimental data and the solid lines correspond to the best curve fit. (h) Schematic diagram of the interfacial interaction between the positive surface charge of the ZnO nanoparticle and the $-CF_2-$ dipoles of the PVDF chain.

applications.[29] Furthermore, the AFM topography image (Fig. 2d), along with the line scan (Fig. 2e), on the PVDF–ZnO composite nanofibers illustrates the mutual adhesion and overlapping of the bunch of nanofibers in the electrospinning process, as marked and separated by consecutive dotted lines. It is worth mentioning that the average fiber diameter was found to be around 147 nm from the AFM topography scan, which is consistent with the results of the SEM image based statistical data analysis. The line scans on several other nanofibers (ESI, Fig. S3†) provide direct evidence that the fiber diameter of an individual fiber is less than 200 nm. As the nanofibers are cylindrical in nature, the fiber diameter can be estimated as the vertical height difference from the substrate. Considering the horizontal distance does not give correct results, as the electrospinning process forces overlapping of the fibers during generation and collection yielding mesoscopic joints and a significantly enhanced mechanical robustness.[28] In most cases, fibers are arranged in groups in which mutual adhesion through formation of these joints takes place. The effect of the ZnO NPs was further observed by the removal of the non-polar α-phase (764 cm^{-1}) and the increment of the electroactive β-(1275 cm^{-1}) and γ-phases (1236 cm^{-1}), as shown in Fig. 2f. The PVDF–ZnO composite nanofibers possess a higher content of electroactive phases (~70%) in comparison to that of the neat PVDF nanofiber (~54%). The electroactive phase content was calculated using the Beer–Lambert law, $F_{EA} = \frac{A_{841}}{\left(\frac{K_{841}}{K_{762}}\right)A_{762} + A_{841}} \times 100\%$ in which, A_{762} and A_{841} represent the absorbencies at 762 and 841 cm^{-1} respectively, $K_{762} = 6.1 \times 10^4$ cm^2 mol^{-1} and $K_{841} = 7.7 \times 10^4$ cm^2 mol^{-1}, representing the absorbance coefficient corresponding to the wavenumbers.[40–42] The electroactive phase content can be further improved with increased amounts of the ZnO nanoparticles, as observed previously.[18] Also, the ZnO NPs improved the degree of crystallinity (χ_{ct}) in the PVDF–ZnO composite nanofibers (~63%) compared to that of the neat PVDF nanofibers (~45%). The degree of crystallinity was evaluated using the well-established curve deconvolution method based on the XRD pattern (Fig. 2g) and calculated using the equation, $\chi_{c_t} = \frac{\sum A_{cr}}{\sum A_{cr} + \sum A_{amr}} \times 100\%$ in which $\sum A_{cr}$ and $\sum A_{amr}$ are the total integral area resulting from the crystalline peaks and the amorphous halo, respectively.[42] The XRD results were found to be in good agreement considering the presence of the electroactive phases and those obtained using Fourier transform infrared spectroscopy (FT-IR) analysis as well. The enhanced electroactive phase content and crystallinity are attributed to the interfacial interaction phenomena[42] between the positive surface charge of the ZnO nanoparticle[43] and the $-CF_2-$ part of the PVDF chain, as depicted schematically in Fig. 2h.

2.3. Ferroelectric and piezoelectric properties

The ferro- and piezo-electric properties of the PVDF–ZnO composite nanofiber were probed using piezoresponse force microscopy (PFM). The atomic force microscope (AFM) topography image is shown in Fig. 3a. It consists of several

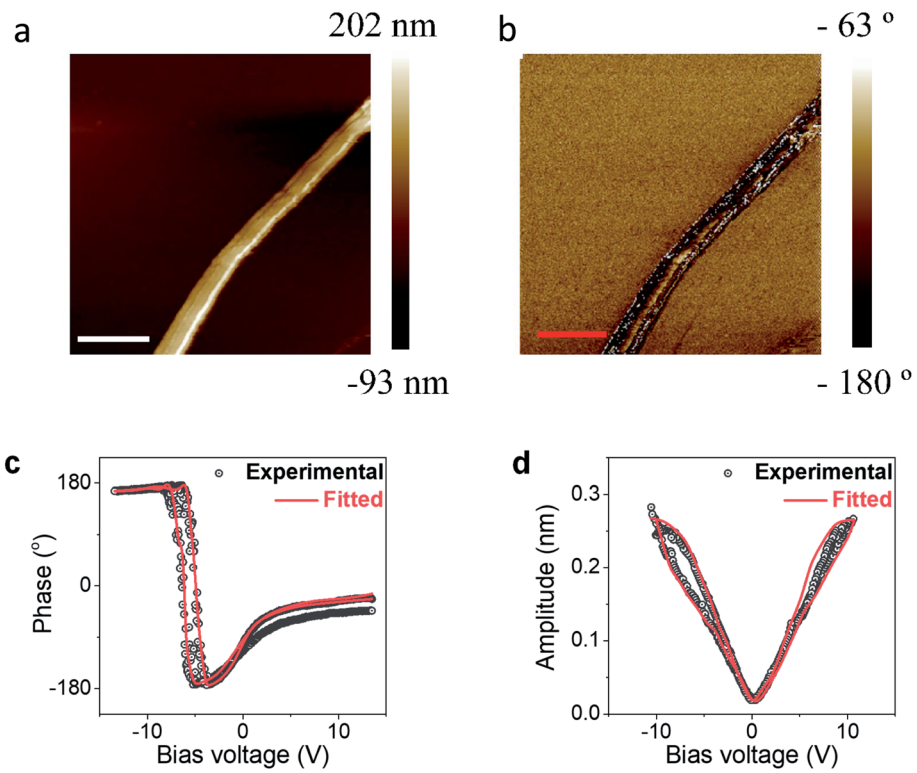

Fig. 3 Measurement of the ferro- and piezo-electricity output of the PVDF–ZnO composite nanofiber using PFM. AFM (scan area: 20 μm × 20 μm) (a) topography image, and (b) phase image (scale bars ~ 5 μm). (c) PFM phase–voltage and (d) the amplitude–voltage butterfly loop.

overlapped nanofibers (with an average diameter of 165 nm) revealing a hump like profile in the line scan profile as shown in Fig. S3a (see ESI†). The corresponding phase image (Fig. 3b) indicates that all dipoles in the middle and along the length of the nanofiber are in-phase, whereas the dipoles at the periphery of the nanofiber are out of phase with respect to the applied AC modulating signal of 6 V, revealing a white and black contrast, respectively. The polarization switching behavior (*i.e.*, ferroelectricity) has been investigated by acquiring the piezoresponse phase *versus* the bias voltage (V_{dc}) hysteresis loop (Fig. 3c), while the DC sweeping voltage was applied to the sample. It was found that the dipolar orientation was switched from 167° (−10 V) to 25° (+10 V) with the gradual increase of V_{dc}. Additionally, a sudden dip close to the switching voltage appeared owing to an internal bias field inside the materials and/or a difference in the work function between the top electrode (Pt coated conducting probe) and the bottom electrode (ITO) and/or the humidity effect (in this case relative humidity ~45%).[44] The difference between the two coercive voltages was found using the equation: $\Delta V_c = V_{c(+)} - V_{c(-)} = 1.373$ V. Furthermore, the electric field stimulated amplitude change (*i.e.*, piezoelectricity) in the PVDF–ZnO composite nanofiber was studied using the amplitude *versus* the applied bias graph featuring the butterfly curve (Fig. 3d). It has been observed that upon increasing and decreasing the bias voltage the amplitude was gradually increased and decreased, respectively, owing to the synchronous elongation and contraction of the nanofibers with the electric field. This is due to the converse piezoelectric effect. Under the applied electrical field, the converse piezoelectric phenomena generates a mechanical strain with a magnitude ε_p within the fiber as, $\varepsilon_p = d_{33}E$, in which E is the applied electric field and d_{33} is the piezoelectric coefficient.[45] The calculated d_{33} coefficient of the PVDF–ZnO composite nanofiber from the slope of the butterfly loop was calculated as −32 pm V^{-1}.

2.4. Piezoelectric energy harvesting

Owing to the stress concentration effect, the PVDF–ZnO composite nanofiber-based A-PNG possesses a significantly enhanced output voltage compared to that of the neat PVDF based A-PNG (shown in Fig. S4, ESI†). Thus, the overall piezoelectric energy harvesting performance of the PVDF–ZnO composite nanofiber-based A-PNG is demonstrated in Fig. 4. Fig. 4a shows the output voltage of 18 V generated from the A-PNG under a pressure amplitude of 18 kPa by repeated movement of a human finger. Further theoretical simulation reveals that the experimentally measured output voltage was almost consistent with the simulated output voltage (ESI, Fig. S5†) which enables our fabricated nanogenerator to be operated according to basic piezoelectric theory. It is important to mention that the working mechanism of the PVDF–ZnO based A-PNG can be properly explained by the synergistic effect between the piezoelectric ZnO nanofillers and the electroactive β-crystals of PVDF.[18] For the neat PVDF based A-PNG, the voltage was generated from the electroactive phases only (~54%). On the other hand, a higher voltage was generated from the PVDF–ZnO based A-PNG owing to the synergistic effects of the higher electroactive phases (~70%) of PVDF, the piezoelectric charges from the ZnO nanoparticles and the stress concentration effect between the ZnO and PVDF, as observed from the theoretical simulation shown in Fig. 1. We can see that an equal amplitude of positive and negative voltages was generated under pressing and releasing the same force because of the switching of the oriented dipoles. The generation of the output voltage from A-PNG depends on the applied input imparting a pressure amplitude because the ionic charge displaced within the crystal structure depends on the applied mechanical energy. The energy harvesting performance of the A-PNG under different pressure amplitude (σ_a) values from 3–18 kPa is shown in Fig. 4b. Here we have applied a finger imparting technique to examine the piezoelectric energy harvesting performance of the PVDF–ZnO composite nanofiber-based A-PNG. The average amplitude of pressure has been applied under human finger imparting, this is consistent with previously reported works.[46–48] The output open-circuit voltages (V_{oc}) were found to increase linearly with the increase in the input pressure, which is consistent with the piezoelectric theory (Fig. 4c).[43] The linear fitting was performed using the equation, $y = 0.98x + 2$, in which the standard error in the slope was 0.233, the Pearson correlation coefficient was 0.9248 and the adjusted R-squared value was 0.80701. We found that an applied pressure amplitude of 18 kPa is sufficient to reach the limiting value of ionic displacement for crystal deformation of our ZnO nanoparticles added PVDF polymer-based energy harvester. Thus, no significant change was found in the output generated voltage when the applied pressure amplitude exceeds 18 kPa. The mechano-sensitivity (S_M), defined as, $S_M = (\Delta V_{oc}/\Delta P)$, has been determined to quantify the dynamic mechanical stimuli sensing ability, in which ΔV_{oc} and ΔP are the differences in the output voltage and pressure respectively.[37] The average mechano-sensitivity (S_M) of the A-PNG is approximately 1.0 V kPa^{-1} over a wide pressure range of (3–18 kPa), which is higher than the previously published high-performance nanogenerators (Table S1, ESI†) owing to the striking role of the ZnO nanoparticle incorporated PVDF nanofibers. Therefore, it is important to mention that our A-PNG can precisely distinguish a small change in the mechanical impact presenting discernible output responses. This result indicates the suitability of using the A-PNG as a sensible self-powered biomedical wearable sensor.

The higher sensitivity of the A-PNG arises as a result of the superior piezoelectric figure of merit FoM $= g_{33}d_{33} = 11.52 \times 10^{-12}$ Pa^{-1} of the PVDF–ZnO composite nanofibers in comparison to the neat PVDF fiber (FoM $= 7 \times 10^{-12}$ Pa^{-1}).[47] Here, the piezoelectric voltage coefficient (g_{33}) was estimated using $g_{33} = \dfrac{d_{33}}{\varepsilon_0\varepsilon_r} = 0.36$ V m N^{-1}, in which, ε_0 is the permittivity of free space (8.85×10^{-12} F m^{-1}) and $\varepsilon_r \approx 10$ is the dielectric constant of the PVDF–ZnO composite nanofibers.[49] Moreover, Fig. 4d shows the output performance of the A-PNG at different frequencies ranging from 1–5 Hz under a constant mechanical

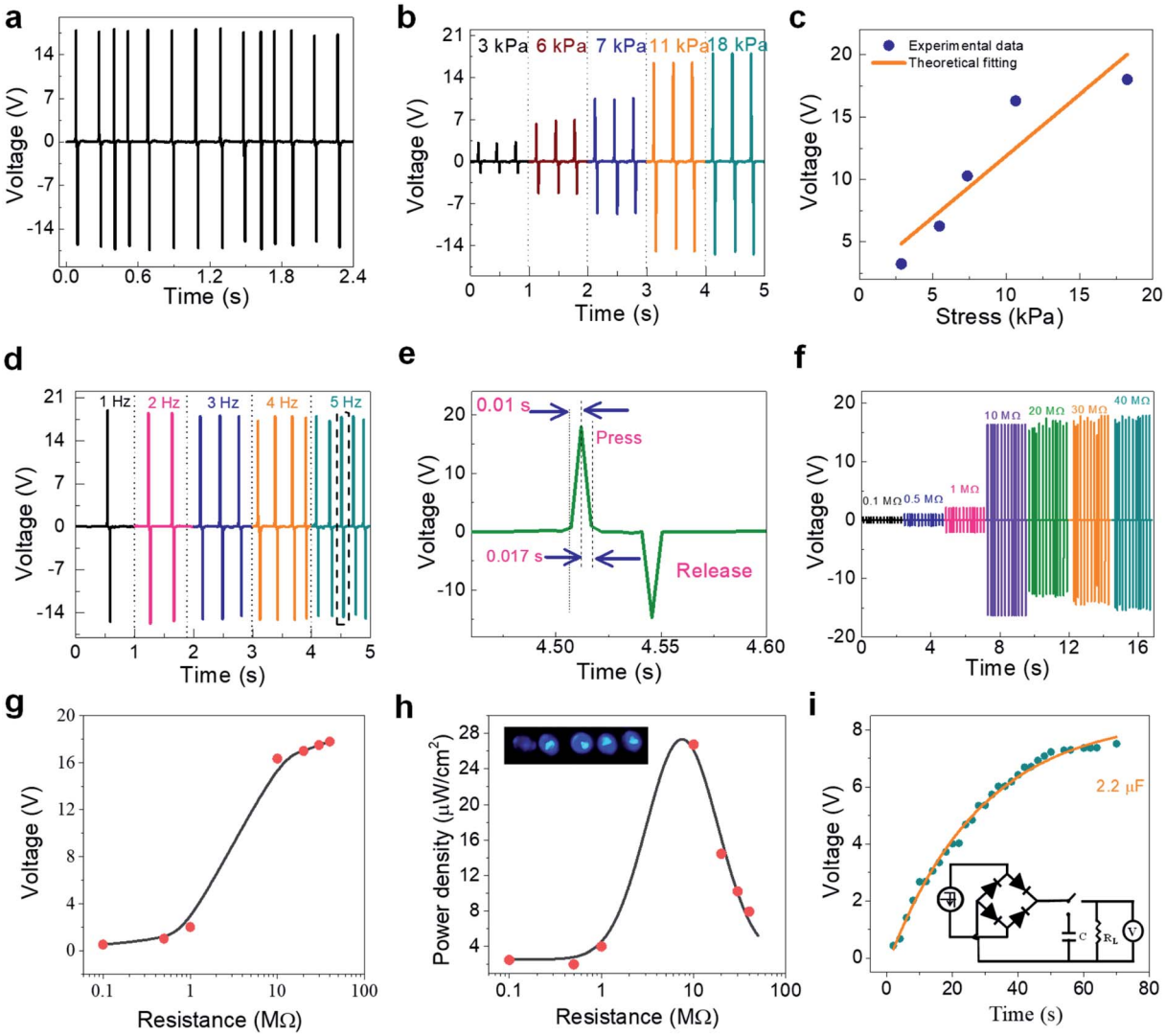

Fig. 4 Energy harvesting characterizations of the PVDF–ZnO composite nanofiber based A-PNG. (a) Measured open-circuit output voltage under a repeated pressure amplitude of 18 kPa. (b) Pressure dependent output voltage. (c) Study of the output voltage with applied pressure. (d) Performance characterization of the A-PNG under different frequency conditions. (e) The expanded view of the output positive voltage (press) and negative voltage (release) pulse signal of the marked cycle in (d). (f) Variation in the output voltage with external load resistances. (g) Study of the nature of the output voltage change with different load resistors. (h) Instantaneous power output as a function of the external load resistance and the glowing array of blue LEDs resulting from direct finger touch as shown in the left and right insets. (i) Capacitor charging performance of the A-PNG. A schematic diagram of the charging and output voltage measurement circuit as a function of the external load is given in the lower right inset.

pressure of 18 kPa. The output signal from the A-PNG is almost constant in the frequency range up to 5 Hz.[49] Interestingly, Fig. 4e shows the expanded view of the positive voltage pulse (press) and the negative voltage (release) signal of the rectangular black dotted marked cycle of Fig. 4d. It was simultaneously found that the voltage pulse increases from zero to its positive peak within a very short period of time, approximately 10 ms, and it returns to zero by approximately 17.0 ms, which indicates the ultra-fast response time of the A-PNG demonstrating that it is the most suitable sensor for ultra-fast signal detection in sensory fabrication. Another way of demonstrating energy harvesting capabilities of the A-PNG is by connecting the device to an external load resistance (R_L). Here, different load resistors (R_L) values were applied to estimate the voltage output and the change in the output voltage with an external load resistor is shown in Fig. 4f under constant pressure conditions ($\sigma_a \sim 18$ kPa). As the load resistance increased, the generated voltage became larger due to Ohm's law which is evident from Fig. 4g. The instantaneous output power density (P) of the A-PNG was calculated as $P = \frac{1}{A}\frac{V_L^2}{R_L}$, in which A is the effective surface area ($\sim$1 cm^2), and V_L is the voltage drop across the load resistance R_L. Fig. 4h displays the variation in the output power density (P) with respect to the load resistance (R_L). As per the result, it was found that the highest instantaneous power density ($P \sim 26.7$ μW cm^{-2}) from the A-PNG was observed at a R_L

of approximately 10 MΩ under repeated human finger imparting conditions at a constant pressure amplitude of $\sigma_a \sim 18$ kPa. Beyond a load resistance of 10 MΩ, the generated power density of A-PNG shows a decreasing trend. This ensures that the 10 MΩ load resistance is the complete load matching resistance to A-PNG needed for obtaining the maximum power density, as described by the maximum transfer power theorem in circuit and network theory, hence $R_L = R_i = 10$ MΩ (internal resistance of the device).[47] The achieved piezoelectric output performance is higher than that of the previously reported all-fiber based nanogenerators (Table S2, ESI†) and also the previously reported PVDF–ZnO composites (Table S3, ESI†). Therefore, our work is superior to previous reports in terms of device and materials aspects. It is noted that this high power output is sufficient to operate an array of five commercially available light-emitting diodes (LEDs) (left upper inset of Fig. 4h) when subject to mechanical pressure without using a storage system. Furthermore, to prove the practical applications of the A-PNG the output voltage was first rectified through a bridge rectifier circuit and used to charge a commercially available capacitor with a maximum capacitance of 2.2 μF under a pressure amplitude of $\sigma_a \sim 18$ kPa. The charging characteristics of the capacitor are shown in Fig. 4i and the corresponding circuit diagram is shown in the inset of Fig. 4i. The A-PNG could charge the capacitor up ($C = 2.2$ μF) to a steady-state voltage of approximately 7.5 V within 70 s. The value of the time constant (τ) for the capacitor is calculated as the time required to recover to $(1 - 1/e)$ or 63% of the steady-state voltage and is approximately 24 s. The capacitor charging performance of the A-PNG is significantly superior to that of the previously reported all-fiber nanogenerators (Table S4, ESI†). Finally, the efficiency (η_{piezo}), as the ratio of the generated output electrical energy (E_{elec}) and the input mechanical energy (W_{mec}), were estimated. The input total mechanical energy per cycle was calculated using: $W_{mec} = F \times \varepsilon \times L = 0.26$ μJ. In which, F is the applied force (∼1.8 N corresponds to $\sigma_a \sim 18$ kPa), ε is the developed axial strain, and the total thickness of the device was $L = 43.5$ μm. The generated axial strain is given by, $\varepsilon = \frac{\sigma_a}{Y} = 3.3 \times 10^{-3}$, in which $Y \sim 5.45$ MPa is the Young's modulus of the PVDF–ZnO composite nanofibres.[50] The optimum resistance (10 MΩ) was connected to the A-PNG to derive the optimized output performance and the output voltage per cycle was measured instantaneously, as shown in Fig. S6, in the ESI.†

$$E_{elec} = \int_{t_1}^{t_2} \frac{V(t)^2}{R} dt$$

The evaluated output energy was found to be $E_{elec} = 0.237 \times 10^{-6}$ J.

Thus, the instantaneous piezoelectric energy conversion efficiency of the A-PNG can be written as $\eta_{piezo} = \frac{E_{elec}}{W_{mec}} \times 100\% = 91\%$ under 18 kPa of pressure amplitude. The energy conversion efficiency of A-PNG is very promising and is superior to previously reported results.[51–54]

2.5. Human physiological signal monitoring

The piezoelectric sensing performance of the A-PNG was further applied to monitor human daily activities. In order to achieve human physiological signal monitoring, the A-PNG was fastened to different parts of the body to record the data depicted in Fig. 5a. For example, the device was attached to the throat. Our device exhibits a reproducible sensing capability with regards to thoracic pressure originating from vibration of the tissue around the vocal cord during repeated coughing actions, as depicted in Fig. 5b. The short-time Fourier transform (STFT) of one coughing signal shows the vocal cord vibration is within 400 Hz, which is consistent with a previous report (see right inset of Fig. 5b).[55] Therefore, the A-PNG can be used as a self-powered sensor to monitor and compare throat or vocal cord related issues for normal human patients.

In addition to that, our designed pressure sensor was adhered to the wrist, just above the radial artery as this area is generally used in arterial tonometry and sphygmography.[56,57] It is important to mention that the most crucial social care should be taken against the prevalence of cardiovascular diseases (CVD) which can be much affected even by COVID-19.[17] Thus, advanced observation and continuous monitoring of arterial blood pressure and heart rate are important. Here, the sensor was used to distinguish the subtle pressure changes between arterial blood pressure in three different situations (as shown in Fig. 5c). From the recorded graphical data analysis wrist pulses (each peak denotes one pulse) under normal rest conditions (∼80 bpm (beats per minute)), after smoking (∼100 bpm) and after running condition (∼110 bpm) were recorded. A more detailed explanation of these three signals is provided in the enlarged view in Fig. 5d and e, in which the health conditions of the same person were analyzed to determine their wellbeing. Here, P_0 represents the diastolic pressure, and the conventional pressure waveforms consist of three peaks, these are $P_1(t_1)$: percussion wave (P-wave), $P_2(t_2)$: tidal wave (T wave) and $P_3(t_3)$: diastolic wave (D-wave), which are generally seen in the diastole region.[56,57] It was noted that due to the superposition of the reflected blood waveform in the lower limb, as well as the emerging blood waveform from the left ventricular contraction, the pulse pressure shape (PPS) was generated. Three main important parameters can be derived from Fig. 5d, such as: (i) the difference in time between the two successive peaks ($\Delta\tau = t_2 - t_1$); and (ii) the radial augmentation index ($AI_r = P_2/P_1$) which was applied as an index for vascular aging related to the diagnosis of arterial stiffness and increased pulse wave velocity (PWV). The average radial augmentation index (AI_r) was found to be 0.65 with a $\Delta\tau$ value of approximately 0.13 s under resting conditions, whereas for smoking conditions, $AI_r = 0.82$ and the $\Delta\tau$ value were approximately 0.14 s, and after running these were $AI_r = 0.87$ and an $\Delta\tau$ value of approximately 0.19 s. The estimated AI_r and $\Delta\tau$ quantities in the static state were found to be in good agreement for an individual in their older twenties, as described by Nichols *via* tonometry and in the previous reports.[57,58] Regarding the above calculated different parameters, it was found that the peak P_2 in the PPS and the AI_r value were reduced during the course of the smoking and running

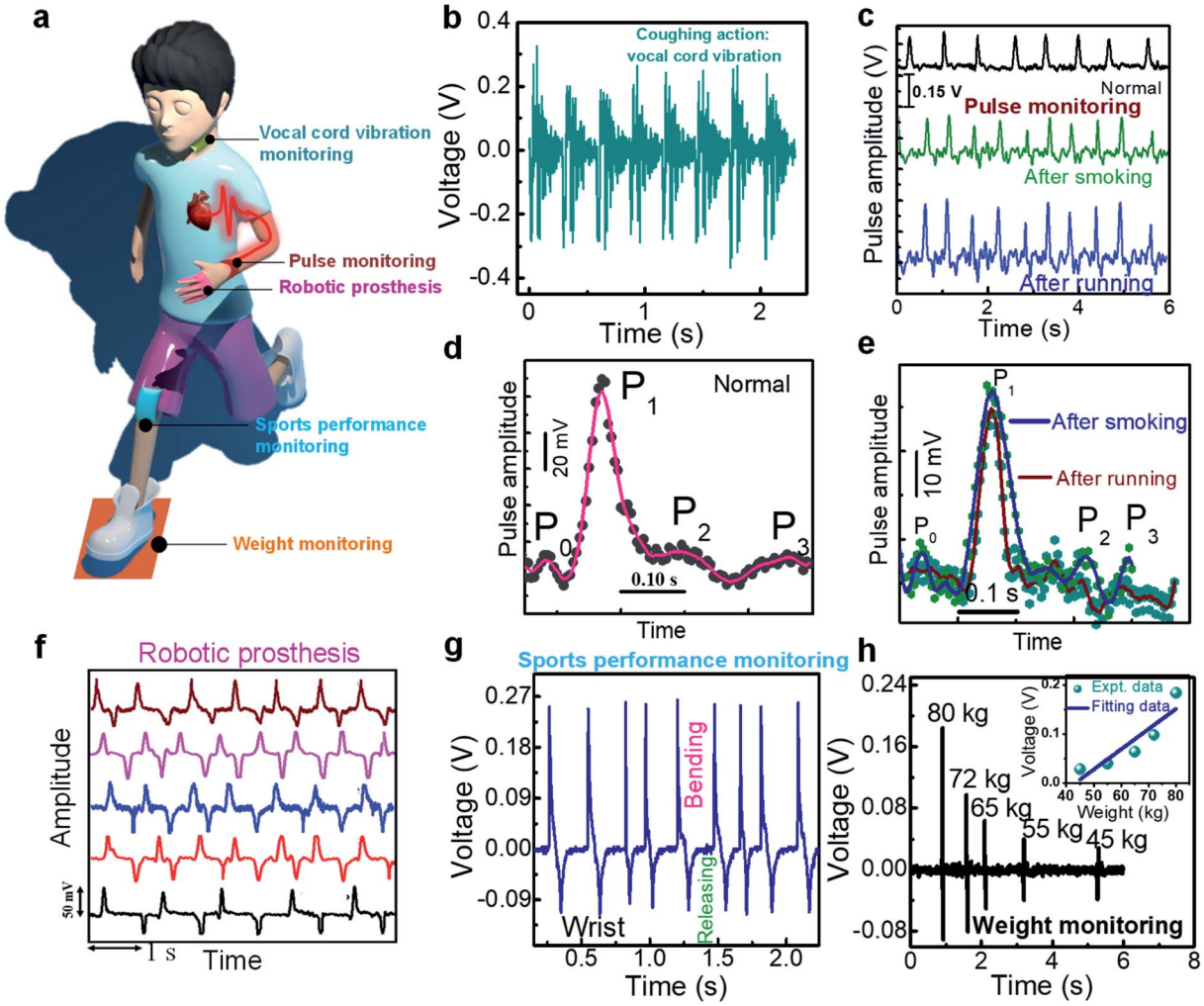

Fig. 5 (a) Real time application of the A-PNG as a self-powered wearable sensor in different parts of the human body for measuring biomedical activity. Output voltage generation from the A-PNG used to monitor different human motions such as (b) vocal cord vibrations: coughing action, (c) pulse monitoring: the radial artery of the wrist, and the enlarged view of a single cycle in (c) are shown in (d) in the normal or rest condition and (e) under smoking and running conditions, respectively. (f) Robotic prosthesis: bending and stretching motions of individual fingers (order from top to bottom: little, ring, middle, index and thumb). (g) Sports performance monitoring: bending and stretching motions of the knee muscles. (h) Weight monitoring: walking/standing on A-PNG.

situation. The estimated value of AI_r was applied as an important parameter to diagnose vascular aging-related issues, as well as being significantly related to the physiological condition of the human cardiovascular system. This shows prospective applications for use as a portable and wearable sensor, enabling real-time human physiological signal monitoring.

Importantly, it is also useful for monitoring ultra-fine physiological signals, such as human finger motions, as shown in Fig. 5f in which it is used as a robotic prosthesis control. In this case, the wearable sensor was smoothly fastened in a particular position on a person's body using medical tape, owing to the very low weight and highly flexibility of the sensor it resulted in minimal restriction to normal skin/body movements. Here the external pressure is applied periodically by different human finger movements to obtain the piezoelectric output response from the A-PNG. To demonstrate the practicability of the A-PNG, it was adhered to human fingers to observe the movement of the fingers and the corresponding voltage output resulting from the bending and stretching motion of each finger was measured. The voltage waveforms produced by different human finger movements were also different, which could enable the movements of a finger to be perceived in a musician's dystonia for example, or to enable the master-hand of a robot to remotely execute surgical procedures (tele-surgery) or to enhance safety and speed in mine clearance activites.[59,60] Thus, the sensor displays distinct patterns of output signals by determining the voltage changes combined with changes in the bending and releasing of all five fingers, which could pave the way towards remote health care monitoring information from sick patients being transmitted to the mobile phones of health workers. Our fabricated device can also be used for monitoring sports performance. As a proof-of-concept, the A-PNG was fixed onto a human knee, as shown in Fig. 5a. The response of the A-PNG on the bending and releasing of the knee muscle with excellent

sensitivity is demonstrated in Fig. 5g. It mimics the motions of the human knee (bending and releasing) leading to a measurable output signal (*i.e.*, voltage). The output response for the physiological signals of human knee motions can be easily tailored to monitor different types of human motions and does not restrict motions, in contrast to conventional rotary encoders, and would therefore be beneficial for user friendly rehabilitation.[61] This sensory information obtained from a wearable A-PNG attached to the skin is helpful for the analysis of body movements in the course of sports activities and exhibits its potential for use as an epidermal device for monitoring the motion of the skin. Therefore, it can be concluded that the A-PNG can be used as a strain sensor to exhibit distinguishable output signals with different patterns related to numerous stimuli from synovial joints, such as the knee.

In addition, the promising and fast output responses of the A-PNG under different forces and pressures has inspired us to fabricate a weight sensor by using A-PNG for weight monitoring. The weight sensing performance of the A-PNG was investigated by recording the output voltage (V_{oc}) under several weights (W in kg). We have characterized five people of different weights and ages in order to assess the weight sensing capabilities. Here, we measured the V_{oc} of a person when they were standing on an A-PNG. The recorded voltage responses for five different people within a weight range of 45–80 kg are shown in Fig. 5h. The variation in the output voltage (V_{oc}) with weight (W) is presented in the right upper inset of Fig. 5h and the graphs have been fitted using the linear equation. It was concluded that the value of V_{oc} increased linearly with W (in kg) in the range of 45–80 kg. Therefore, it is worth mentioning that the unknown weight of any person lying between 45 and 80 kg can be predicted by measuring the V_{oc} only with the developed device. Overall, the A-PNG has been successfully demonstrated as an ultrasensitive healthcare monitoring sensor that can report a wide range of health status information.

3. Conclusions

In summary, we have demonstrated an all-fiber ZnO-nanoparticles confined stress amplified PVDF electrospun nanofibers based piezoelectric nanogenerator that demonstrates an excellent performance to harvest mechanical energy from human movements. The electrospinning process enables simple, low-cost, scalable and large-scale production of composite piezoelectric nanofibers. In addition, a high fraction of the piezoactive β-phase is induced which indicates a further processing step, therefore a post electrical poling treatment can be avoided. Finite element analysis of the stress distribution showed that a significant amount of external stress is concentrated to deform the ZnO nanoparticles, improving the stress-induced large polarization in the PVDF–ZnO composite nanofibers, thus allowing effective generation of electricity. The nanogenerator made using ZnO-nanoparticles embedded in PVDF composite nanofibers exhibits an open-circuit output voltage up to approximately 18 V when an applied pressure amplitude of approximately 18 kPa is imparted with a 91% energy harvesting efficiency. The A-PNG shows a fast response time of 10 ms under an imparting frequency of 5 Hz which is the most suitable for fast signal detection in sensory systems. The PVDF–ZnO composite nanofibers possesses an enhanced piezoelectric charge coefficient $d_{33} = -32$ pC N^{-1} and a superior figure of merit FoM $\approx 11.52 \times 10^{-12}$ Pa^{-1} compared to a neat PVDF nanofiber-based nanogenerator. As a result, the device can successfully operate several consumer electronic devices. Owing to the fast response time, the device is suitable for use in human physiological signal monitoring applications. The adaptability of the fabricated sensor makes it easy and comfortable to wear or adhere to the human body and shows promise for application of the device for the constant monitoring of respiratory and pulse data from patients.

4. Experimental

4.1. Materials

The following materials were obtained, poly(vinylidene fluoride) (PVDF) pellets ($\bar{M}_w \sim 275\,000$, Sigma-Aldrich, USA). ZnO-nanoparticles (99% of purity and particle size $\sim$ 70 nm), *N*,*N*-dimethyl formamide (DMF, 99.5% of purity), acetone (Merk Chemical, India), and Ni–Cu plated polyester fabric (DE2-280C, EMS Inc., Korea). All materials were utilized without any further purification.

4.2. Synthesis of the ZnO nanoparticles

In order to synthesize the ZnO nanoparticles, stock solutions of $Zn(CH_3COO)_2 \cdot 2H_2O$ (0.1 M) were prepared in 50 ml deionized (D.I.) water under vigorous stirring. To this stock solution, 25 ml of NaOH (0.5 M) solution prepared in D.I. water was added under continuous stirring in order to obtain reactants with pH values between 8 and 11. These solutions were transferred into Teflon lined sealed stainless steel autoclaves and the temperature was maintained at 120 °C for 12 h under autogenous pressure. It was then allowed to cool naturally to room temperature. After the reaction was completed, the resulting white solid products were washed with D.I. water three times, filtered and then dried in air in a laboratory oven at 60 °C for 12 h.

4.3. Fabrication of the electrospun nanofibers

To prepare a PVDF solution (12 wt%), PVDF was dissolved in a mixture of DMF and acetone (mass ratio of 6 : 4) at 60 °C and magnetically stirred for 2 d. Afterwards, the 0.5 wt% ZnO-nanoparticles were added to the PVDF–DMF and acetone solution and magnetic stirring was continued for 2 d. The homogeneous solution was then transferred into a hypertonic syringe with a 0.8 mm diameter needle for electrospinning. The homogeneous solution was placed in a 10 ml plastic syringe fitted with a stainless steel needle with tip-dimensions of 1.20 × 38 mm. A high-voltage power supply (10 to 12 kV) was applied to the solution with respect to the collector, and the distance between the nozzle and the collector was varied from 12 to 14 cm. A syringe pump was used to feed the polymer solution into the needle tip at a rate of 0.6 ml h^{-1}. All experiments were performed at room temperature and at a relative humidity of 43 ± 5%. To obtain a stable nanofibers mat, we allowed the fresh composite electrospun nanofibers mat (shown in the inset of

Fig. S2, ESI†) to dry at 60 °C for 12 h to eliminate the remaining solvents prior to characterization and fabrication of the device.

4.4. Fabrication of all-fibers A-PNG

The details of the fabrication process of our proposed all-fibers A-PNG have been discussed in the results and discussion section and details of the device structure are shown in Fig. 2a. Here, a copper (Cu)–nickel (Ni) plated interlocked micro-fiber-based polyester fabric was used as the top and bottom electrodes, and PVDF–ZnO composite nanofibers were used as an active layer. Finally, the A-PNG was further encapsulated with PDMS (Sylgard 184, Dow Corning Corp., USA) for protection from environmental hazards such as, dust and water and to give a compact structure to the fabricated device. The thickness of the PVDF–ZnO composite nanofibers mat was approximately 3.5 μm and the effective contact area of the A-PNG was 1 cm^2. The total thickness of the device is 43.5 μm. The PDMS encapsulation was prepared by mixing the base and curing agents at a ratio of 10 : 1 and this was placed in a vacuum desiccator to eliminate air bubbles. A pair of conducting copper wires was attached to the top and bottom electrode to enable connection of an external circuit.

4.5. Characterization

The XRD patterns and the crystalline phases of the composite nanofibers were obtained using an X-ray diffractometer (Bruker, D8 Advance) with a Cu K_α ($\lambda_{inc} \approx 1.54$ Å) radiation source under an operating voltage and current of 40 kV and 40 mA, respectively. The crystalline phases of the composite nanofibers were further confirmed using the FT-IR (Bruker, Tensor II) results. The morphologies of the electrospun nanofibers were observed using FE-SEM (FEI, INSPECT F50) operated at an acceleration voltage of 20 kV. The vertical piezoresponse of the fabricated ZnO-PVDF composite nanofiber was probed using a Pt coated conducting probe ($k = 3$ N m^{-1}) in an AFM (Bruker Multimode 8) equipped with a built-in lock in amplifier and SAM III voltage amplifier module. 6 V of AC modulating voltage was applied to the probe and the corresponding lock-in frequency was selected as 12 kHz. The TEM images were recorded at 200 kV (JEM 2100, JEOL). Image J software was used to measure the diameters of the electrospun nanofibers. The repeating human finger touch and release responses and the bio-signal response were recorded in terms of the open-circuit output voltage from the nanogenerator using a digital storage oscilloscope (Agilent, DSO3102A). The capacitor charging performance was obtained using a typical rectifier bridge circuit unit. All measurements were carried out at room temperature.

Conflicts of interest

The authors declare no competing financial interest.

Acknowledgements

This work was financially supported by a grant from the Department of Science and Technology (DST/TMD/MES/2K17/91), Government of India.

References

1 R. Zhang, M. Hummelgård, J. Örtegren, Y. Yang, H. Andersson, E. Balliu, N. Blomquist, M. Engholm, M. Olsen, Z. L. Wang and H. Olin, *Nano Energy*, 2019, **63**, 103842–103851.
2 T. He, H. Wang, J. Wang, X. Tian, F. Wen, Q. Shi, J. S. Ho and C. Lee, *Adv. Sci.*, 2019, **6**, 1901437.
3 Y. Ma, Q. Zheng, Y. Liu, B. Shi, X. Xue, W. Ji, Z. Liu, Y. Jin, Y. Zou, Z. An, W. Zhang, X. Wang, W. Jiang, Z. Xu, Z. L. Wang, Z. Li and H. Zhang, *Nano Lett.*, 2016, **16**, 6042–6049.
4 T. Q. Trung and N.-E. Lee, *Adv. Mater.*, 2016, **28**, 4338–4372.
5 Y. Khan, A. E. Ostfeld, C. M. Lochner, A. Pierre and A. C. Arias, *Adv. Mater.*, 2016, **28**, 4373–4395.
6 D.-H. Kim, N. Lu, R. Ma, Y.-S. Kim, R.-H. Kim, S. Wang, J. Wu, S. M. Won, H. Tao, A. Islam, K. J. Yu, T.-I. Kim, R. Chowdhury, M. Ying, L. Xu, M. Li, H.-J. Chung, H. Keum, M. McCormick, P. Liu, Y.-W. Zhang, F. G. Omenetto, Y. Huang, T. Coleman and J. A. Rogers, *Science*, 2011, **333**, 838–843.
7 M. Kaltenbrunner, T. Sekitani, J. Reeder, T. Yokota, K. Kuribara, T. Tokuhara, M. Drack, R. Schwödiauer, I. Graz, S. Bauer-Gogonea, S. Bauer and T. Someya, *Nature*, 2013, **499**, 458–463.
8 C.-L. Choong, M.-B. Shim, B.-S. Lee, S. Jeon, D.-S. Ko, T.-H. Kang, J. Bae, S. H. Lee, K.-E. Byun, J. Im, Y. J. Jeong, C. E. Park, J.-J. Park and U.-I. Chung, *Adv. Mater.*, 2014, **26**, 3451–3458.
9 G. Schwartz, B. C.-K. Tee, J. Mei, A. L. Appleton, D. H. Kim, H. Wang and Z. Bao, *Nat. Commun.*, 2013, **4**, 1859–1866.
10 C. M. Boutry, A. Nguyen, Q. O. Lawal, A. Chortos, S. Rondeau-Gagné and Z. Bao, *Adv. Mater.*, 2015, **27**, 6954–6961.
11 S. C. B. Mannsfeld, B. C.-K. Tee, R. M. Stoltenberg, C. V. H.-H. Chen, S. Barman, B. V. O. Muir, A. N. Sokolov, C. Reese and Z. Bao, *Nat. Mater.*, 2010, **9**, 859–864.
12 S. Yun, S. Park, B. Park, Y. Kim, S. K. Park, S. Nam and K.-U. Kyung, *Adv. Mater.*, 2014, **26**, 4474.
13 G. Zhu, W. Q. Yang, T. Zhang, Q. Jing, J. Chen, Y. S. Zhou, P. Bai and Z. L. Wang, *Nano Lett.*, 2014, **14**, 3208–3213.
14 W. Gao, S. Emaminejad, H. Y. Y. Nyein, S. Challa, K. Chen, A. Peck, H. M. Fahad, H. Ota, H. Shiraki, D. Kiriya, D.-H. Lien, G. A. Brooks, R. W. Davis and A. Javey, *Nature*, 2016, **529**, 509–514.
15 S. Gong, W. Schwalb, Y. Wang, Y. Chen, Y. Tang, J. Si, B. Shirinzadeh and W. Cheng, *Nat. Commun.*, 2014, **5**, 3132–3139.
16 Y. Mao, P. Zhao, G. McConohy, H. Yang, Y. Tong and X. Wang, *Adv. Energy Mater.*, 2014, **4**, 1301624.
17 S. K. Ghosh and D. Mandal, *J. Mater. Chem. A*, 2021, **9**, 1887.
18 J. Li, S. Chen, W. Liu, R. Fu, S. Tu, Y. Zhao, L. Dong, B. Yan and Y. Gu, *J. Phys. Chem. C*, 2019, **123**, 11378–11387.
19 X. Wang, H. Zhang, L. Dong, X. Han, W. Du, J. Zhai, C. Pan and Z. L. Wang, *Adv. Mater.*, 2016, **28**, 2896–2903.
20 H. Chen, C. Xing, Y. Li, J. Wang and Y. Xu, *Sustainable Energy Fuels*, 2020, **4**, 1063–1077.

21 B. Mahanty, K. Maity, S. Sarkar and D. Mandal, *AIP Conf. Proc.*, 2020, **2265**, 030655, DOI: 10.1063/5.0016777.
22 D. Olmos ; G. González-Gaitano ; R. Vela ; L. Córdoba ; J. González-Benito and A. L. Kholkin, *Proceedings of ISAF-ECAPD-PFM 2012*, Aveiro, 2012, pp. 1–3, DOI: 10.1109/ISAF.2012.6297828.
23 R. G. Multhaupt, *Ferroelectrics*, 1987, **75**, 385–396.
24 S. Crossley and S. Kar-Narayan, *Nanotechnology*, 2015, **26**, 344001–344008.
25 S. Jana, S. Garain, S. Sen and D. Mandal, *Phys. Chem. Chem. Phys.*, 2015, **17**, 17429–17436.
26 S. K. Ghosh, T. K. Sinha, B. Mahanty, S. Jana and D. Mandal, *J. Appl. Phys.*, 2016, **120**, 174501.
27 M. Yao, Y. Cheng, Z. Zhou and M. Liu, *J. Mater. Chem. C*, 2020, **8**, 14–27.
28 L. Persano, C. Dagdeviren, Y. Su, Y. Zhang, S. Girardo, D. Pisignano, Y. Huang and J. A. Rogers, *Nat. Commun.*, 2013, **4**, 1633.
29 S. K. Ghosh and D. Mandal, *Nano Energy*, 2018, **53**, 245–257.
30 A. P. Indolia and M. S. Gau, *J. Polym. Res.*, 2013, **20**, 1246.
31 M. Xiong, G. Gu, B. You and L. Wu, *J. Appl. Polym. Sci.*, 2003, **90**, 1923–1931.
32 M. Kim, Y. S. Wu, E. C. Kan and J. Fan, *Polymers*, 2018, **10**, 745.
33 B. Sun, X. Li, R. Zhao, H. Ji, J. Qiu, N. Zhang, D. He and C. Wang, *J. Mater. Sci.*, 2019, **54**, 2754–2762.
34 R. S. Sabry and A. D. Hussein, *Polym. Test.*, 2019, **79**, 106001.
35 S. Bairagi and S. W. Ali, *Int. J. Energy Res.*, 2020, **44**, 1–19.
36 B. –S. Lee, B. Park, H. –S. Yang, J. W. Han, C. Choong, J. Bae, K. Lee, W. –R. Yu, U. Jeong, U. –I. Chung, J. –J. Park and O. Kim, *ACS Appl. Mater. Interfaces*, 2014, **6**, 3520–3527.
37 G. Stan, C. V. Ciobanu, P. M. Parthangal and R. F. Cook, *Nano Lett.*, 2007, **7**, 3691–3697.
38 J. Park, Y. Lee, M. H. Barbee, S. Cho, S. Cho, R. Shanker, J. Kim, J. Myoung, M. P. Kim, C. Baig, S. L. Craig and H. Ko, *Adv. Mater.*, 2019, **31**, 1808148.
39 K. I. Park, S. Xu, Y. Liu, G. T. Hwang, S. J. L. Kang, Z. L. Wang and K. J. Lee, *Nano Lett.*, 2010, **10**, 4939–4943.
40 K. Roy, S. Jana, Z. Mallick, S. K. Ghosh, B. Dutta, S. Sarkar, C. Sinha and D. Mandal, *Langmuir*, 2021, **37**, 7107–7117.
41 B. Mahanty, S. K. Ghosh, S. Garain and D. Mandal, *Mater. Chem. Phys.*, 2017, **186**, 327–332.
42 S. K. Ghosh, M. M. Alam and D. Mandal, *RSC Adv.*, 2014, **4**, 41886–41894.
43 K.-M. Kim, M.-H. Choi, J.-K. Lee, J. Jeong, Y.-R. Kim, M.-K. Kim, S.-M. Paek and J.-M. Oh, *Int. J. Nanomed.*, 2014, **9**, 41–56.
44 M. Park, Y. Y. Choi, J. Kim, J. Hong, H. W. Song, T. H. Sung and K. No, *Soft Matter*, 2012, **8**, 1064–1069.
45 S. K. Ghosh, P. Adhikary, S. Jana, A. Biswas, V. Sencadas, S. D. Gupta, B. Tudu and D. Mandal, *Nano Energy*, 2017, **36**, 166–175.
46 B. Mahanty, S. Ghosh, K. Maity, K. Roy, S. Sarkar and D. Mandal, *Mater. Adv.*, 2021, **2**, 4370–4379.
47 B. Mahanty, S. K. Ghosh, S. Jana, K. Roy, S. Sarkar and D. Mandal, *Sustainable Energy Fuels*, 2021, **5**, 1003–1013.
48 S. K. Ghosh, T. K. Sinha, B. Mahanty and D. Mandal, *Energy Technol.*, 2015, **3**, 1190–1197.
49 P. I. Devi and K. Ramachandran, *J. Exp. Nanosci.*, 2011, **6**, 281–293.
50 F. Mokhtari, M. Shamshirsaz, M. Latif and S. Asadi, *J. Text. Inst.*, 2017, **108**, 906–914.
51 J. Fang, X. Wang and T. Lin, *J. Mater. Chem.*, 2011, **21**, 11088–11091.
52 S. K. Ghosh, K. Roy, H. K. Mishra, M. R. Sahoo, B. Mahanty, P. N. Vishwakarma and D. Mandal, *ACS Sustainable Chem. Eng.*, 2020, **8**, 864–873.
53 M. Pusty and P. M. Shirage, *RSC Adv.*, 2020, **10**, 10097–10112.
54 S. K. Ghosh, T. K. Sinha, M. Xie, C. R. Bowen, S. Garain, B. Mahanty, K. Roy, K. Henkel, D. Schmeißer, J. K. Kim and D. Mandal, *ACS Appl. Electron. Mater.*, 2021, **3**, 248–259.
55 P. Piirila and A. R. A. Sovijarvi, *Respir. J.*, 1995, **8**, 1949–1956.
56 A. P. Avolio, M. Butlin and A. Walsh, *Physiol. Meas.*, 2010, **31**, R1–R47.
57 W. W. Nichols, *Am. J. Hypertens.*, 2005, **18**, 3S–10S.
58 S. K. Ghosh, J. Park, S. Na, M. P. Kim and H. Ko, *Adv. Sci.*, 2021, 2005010, DOI: 10.1002/advs.202005010.
59 E. J. Hanly and M. A. Talamini, *Am. J. Surg.*, 2004, **188**, 19S–26S.
60 S. Jana, S. Garain, S. K. Ghosh, S. Sen and D. Mandal, *Nanotechnology*, 2016, **27**, 445403–445415.
61 J. Nikitczuk, B. Weinberg and C. Mavroidis, *Smart Mater. Struct.*, 2007, **16**, 418–428.

